

High sensitive room temperature ammonia sensor based on dopant free m-WO₃ nanoparticles: Effect of calcination temperature

M. S. Duraisami*, K. Parasuraman

PG & Research Department of Physics, Poompuhar College (Autonomous), Melaiyur – 609107, Tamilnadu, India
Affiliated to Bharathidasan University, Tiruchirappalli

*tharmamithran@gmail.com

PACS 07.07.Df, 81.07.b, 61.46-w, 61.46.Hk, 61.72Uj, 61.82.Rx DOI 10.17586/2220-8054-2020-11-5-578-589

In this article, monoclinic tungsten tri-oxide (m-WO₃) nanoparticles (hereafter NPs) were prepared by facile precipitation method and they were successfully examined as gas sensing materials for monitoring gaseous ammonia at room temperature have been reported. The effect of calcination temperature on structural and morphological properties of the prepared samples were also investigated. Physicochemical properties of the samples were characterized by XRD, SEM, XPS, UV-Vis and PL analysis. XRD studies confirmed the monoclinic structure of the prepared NPs. Optical studies disclosed that the obtained samples were having wider optical band gaps ranging from 2.48 to 2.76 eV. Sensing signatures such as selectivity, transient response along with performance indicators like repeatability and stability have also been investigated. Involving, the sample calcined at 823 K exhibited highly improved sensing response of 142 towards 200 ppm of ammonia with rapid response/recovery time of 26 / 79 s.

Keywords: ammonia sensor, tungsten trioxide, nanoparticles, calcination, precipitation.

Received: 11 June 2020

Revised: 13 September 2020

Final revision: 23 September 2020

1. Introduction

One of the serious challenges we face in recent times is that living environment is losing its stability as a result of the toxic gases released from several industries. According to the statistic survey of WHO, 4 out of 10 most common causes of death are due to respiratory related ailments [WHO, World Health Statistic, 2011]. Toxic gases may often contribute to adverse effects in humans and also their occurrence in environment poses severe threats. Therefore, if the living environment is to be maintained well, it is necessary to detect the leakage of harmful gases at lower concentrations. Among the toxic gases, ammonia is highly reactive and soluble alkaline gas which is present in the environment at ppb levels [1]. The permissible long (8 hour) and short (10 minutes) term exposure limits for ammonia in human are 25 and 35 ppm [2–4]. Due to the demand for fertilizers, ammonia be the second largest chemical product manufactured in the world. Despite its uses, sensing ammonia is an essential process owing to its lethal behavior at higher concentrations [5]. Significantly, ammonia sensors attracted more attention for realizing their applications in various fields like petrochemicals, food and beverage, agriculture, automotive industry, fertilizers and medical applications [6].

One of the most appropriate candidates in the field of toxic gas detection is chemiresistive sensor. In which semi-conducting metal oxide (SMO) nanostructures have been investigated extensively in the fabrication of distinctive gas sensors due to their tunable transport properties [7]. Among the SMOs, WO₃ is a notable well known n-type semiconductor with a wide range of band gap varies from 2.2 to 2.8 eV [8]. Llobet et al. [9] have studied WO₃ nanostructures as an excellent gas sensing material towards reducing gases like ammonia. Moreover, WO₃ nanostructures play a key role in the preparation of colloidal quantum dot LEDs [10], bio sensing electrodes [11] and used in the fields of mechanochemical [12], field emission devices, electrochromic and photocatalysts [13]. Wang et al. [14] have studied WO₃ nanofibers for ammonia gas detection at an operating temperature of 623 K. Wu et al. [15] reported an ammonia sensor based on graphene/PANI nanocomposite with a response of about 11 for 100 ppm. Liu et al. [16] have studied the Ag-decorated Titanium oxide quantum dot clusters for ammonia detection at room temperature. Recently Wang et al. [17] have investigated the gas sensing performance of closely packed WO₃ microspheres for ammonia detection with a response of 3.2 towards 100 ppm ammonia. Tai et al. [18] used PANI/Titanium oxide nanocomposite to detect 117 ppm of ammonia gas at 298 K. Li et al. [19] reported the ZnO thin film as ammonia sensor with a maximum response of 57.5 towards 600 ppm at 423 K.

However, various interpretations were reported for sensing ammonia, still high sensitive ammonia sensors based on undoped SMO at room temperature is rare. For this objective, the present study is primarily aimed to explore the improved gas sensing performances of undoped WO₃ NPs synthesized by a facile precipitation process. The

precipitation method is a well facilitated and self-styled technique as well as envisioned to be one of the most reliable methods for the preparation of nano sized WO_x particles with different morphologies [20]. We are considering the effect of calcination temperature on crystal structure and morphology of the NPs as one of the key factors to improve sensing performance. On these grounds, we prepared WO₃ NPs under various calcination temperatures such as 623, 723, 823 and 923 K. Thus the prepared NPs were used as redox sensors to monitor ammonia gas.

2. Materials and methods

2.1. Synthesis of WO₃ NPs

All the analytical grade chemicals were procured from Sigma–Aldrich and used without further purification. In a typical precipitation procedure, 1.2 millimole of sodium tungstate dihydrate (Na₂WO₄·2H₂O, 99.9 %) and 2 millimole of calcium chloride dihydrate (CaCl₂·2H₂O, 99.9 %) were prepared separately using 100 ml of de-ionized water (DI). Then these two solutions were mixed under vigorous magnetic stirring (900 rpm) for 45 minutes at room temperature. Thereafter, the resulting white precipitate was collected, washed many times with ethanol, acetone and DI, and dried at 333 K for 16 hours using hot air oven. Then, the dried material was soaked in 50 ml of concentrated nitric acid (HNO₃, ≥99 %) for 48 hours resulting yellow precipitates were obtained. These yellow precipitates were cleansed several times with ethanol, acetone and DI. Finally the substance was placed in muffle furnace and calcined at 623 K for 2 hours to improve crystallinity. After the completion of thermal treatment the sample has been ground to acquire fine WO₃ NPs. The similar procedure is followed to the remaining three different calcination temperatures (723, 823 and 923 K).

2.2. Reaction scheme

Figure 1 depicts the schematic representation of WO₃ NPs synthesis procedure. An intermediate substance CaWO₄ was first formed by vigorous stirring of the precursor mixture (Na₂WO₄ and CaCl₂). The Ca²⁺ cations (Lewis acid-electron-pair acceptor) might interact with the WO₄²⁻ anions (Lewis base-electron-pair donor), resulting in the formation of white CaWO₄ precipitates. Then, CaWO₄ was decomposed slowly upon solution acidification to form yellow tungstite (WO₃·H₂O) precipitates. The liberated H⁺ ions from the strong oxidizing agent HNO₃ serve as one of the reactants for the formation of WO₃·H₂O. Remnants were removed by further cleansing process. On the post calcination treatment, WO₃·H₂O gets transformed to WO₃ nanostructures.

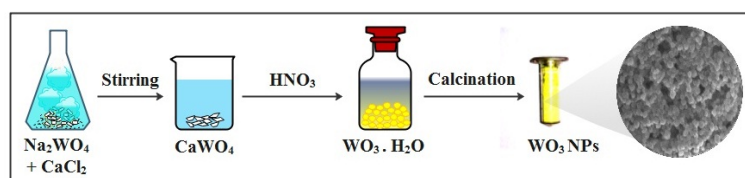
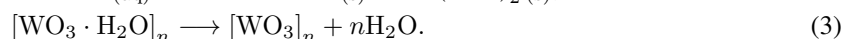
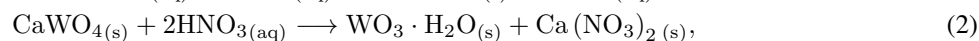
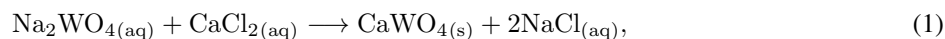


FIG. 1. Schematic representation of WO₃ NPs synthesis procedure

This can be explained as follows; the removal of internal water molecules and W=O double bonds permit the layers to connect through the oxygen atoms to stack together and turn to more compact structure [21]. The possible formation process of WO₃ NPs can be explained as given in Eq. (1), (2) and (3).



2.3. Characterization techniques

The Crystalline structure of the prepared samples was employed using the XRD patterns obtained from Panalytical Xpert-pro Diffractometer with a source of CuKα₁ (λ = 1.5406 Å). The surface morphology of the obtained NPs was analysed using Scanning Electron Microscope (ZEISS-SEM) and Transmission Electron Microscopy (TEM-Hitachi H-9500). EDS (Bruker) analysis was performed to identify the elemental composition of the sample. Electronic state of the elements within the samples was identified using X-ray Photoelectron Spectrometer (Thermo Fisher Scientific Inc., K Alpha, USA). The spectral observations from Fourier Transform Infrared Spectroscopy (Perkin-Elmer Spectrum Two, USA) and Ultraviolet-Visible spectrophotometer (Perkin-Elmer Lambda 35 Spectrophotometer, USA) have given the interpretations about the presence of functional groups and the optical characteristics of the NPs respectively.

The Photo Luminescence spectra of the prepared NPs were recorded at room temperature using Varian Cary Eclipse Spectrophotometer with the scan rate of 600 nm/min.

2.4. Fabrication of gas sensing setup and measurements

All the sensing measurements have been taken at room temperature using a high resistance electrometer (Keithley 6517A, USA) with an integrated gas measurement setup as depicted in Fig. 2. Initially the prepared NPs were dispersed in an appropriate amount of isopropyl alcohol and drop casted on the surface of a glass plate, hence a widespread layer was formed and acts as a sensing material. In it, two copper electrodes have been attached with an applied DC voltage of 10 V. The entire gas sensing process was carried out in the customized evaporation chamber of 1 L capacity. When a liquefied analyte like ammonia was injected in to the evaporation chamber using a micropipette, which swiftly turned in to vapor state and made a contact with the sample. The steady-state baseline resistance (R_a) in air ambience and the variation of electrical resistance from R_a to R_g (resistance under the exposure of target gas) were measured by a highly efficient electrometer (Keithley 6517B, USA) controlled by a personal computer. The concentrations of the analytes to be injected were calculated using static liquid-gas distribution method (Eq. (4)) [22]:

$$C_{(p p m)} = \frac{\delta V_{\Gamma} R T}{M P_b V_b} \times 10^6, \quad (4)$$

where C is the concentration of test vapor (ppm), δ is the density of test vapor (gmL^{-1}), V_{Γ} is the volume of injected vapor (μL), R is the universal gas constant ($8.3145 J \cdot mol^{-1} K^{-1}$), T is the absolute temperature (K), M is the molecular weight, P_b is the chamber pressure (atm) and V_b is the volume of the chamber (L). Generally, for reducing gases, the sensing responses were calculated by the given relation (Eq. (5)) [22]:

$$S = \frac{R_a}{R_g}, \quad (R_a \gg R_g) \quad (5)$$

where R_a and R_g are the resistances of the sample in dry air and target gas.

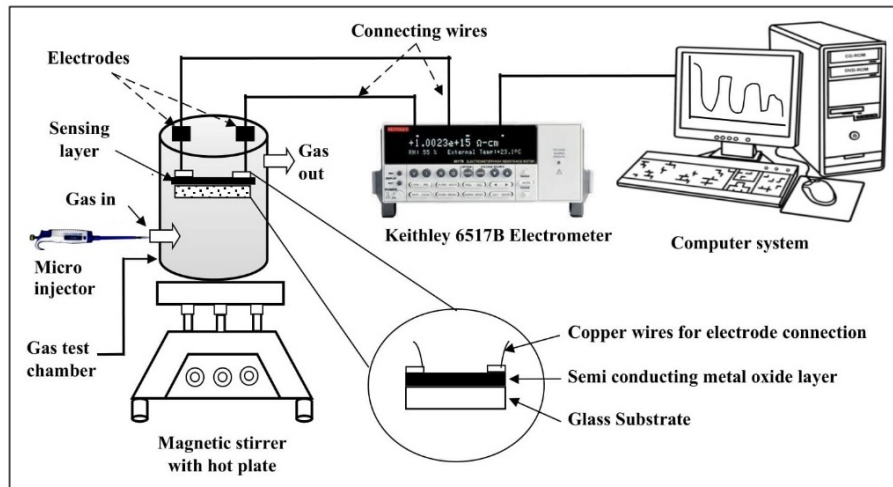


FIG. 2. Illustration of an integrated gas measurement setup

3. Results and discussion

3.1. Structural, morphological and functional groups

Figure 3 shows the XRD pattern of all the synthesized WO_3 NPs. As the calcination temperature increases from 623 to 823 K, the crystallinity comes up gradually and the emergence of different peaks have been observed. Three characteristic diffraction peaks (triplet) for WO_3 were observed from the crystal planes (002), (020) and (200). These peaks are matched well with the observed XRD patterns (standard JCPDS data card no. 43-1035). The samples were crystallized with the polycrystalline monoclinic phase with the lattice parameters $a = 7.297$, $b = 7.539$, $c = 7.688$ Å. The well-known Debye–Scherrer formula is used to determine the average crystallite size (D) of the samples as given in Eq. (6):

$$D = \frac{K\lambda}{\beta \cos \theta}, \quad (6)$$

where K is Scherrer constant (0.89), β – full width at half maximum of the high intensity peak (FWHM in radians), θ – Bragg angle, λ is wavelength of the X-rays (1.5406 Å for $\text{CuK}\alpha_1$). It is observed that, the predominant facet was varied as a function of calcination temperature, therefore the average crystallite size was calculated from triplet peaks, however, which is inappropriate for 623 K sample due to its partial crystalline nature. The mean crystallite size found to be increase in the range of 17 to 39 nm with increased calcination temperature. This trend implies that higher temperature provided adequate energy for smaller particles to coalesce into larger ones. It is clearly known from XRD studies that there is no influence of any other characteristic peaks of impurities were observed, hence WO_3 NPs were formed without any impurities.

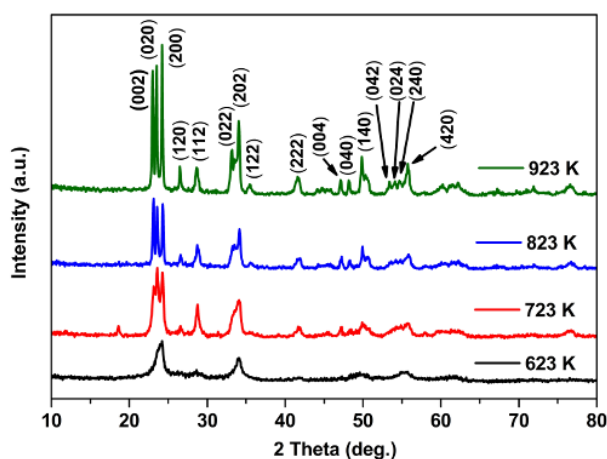


FIG. 3. X-ray diffraction patterns of the synthesised WO_3 samples

The SEM images and size distribution histograms for the prepared samples are shown in Fig. 4. Invitingly, the morphology was improved with increased calcination temperature from 623 to 823 K. Uniformly distributed fine cluster like nanogranular morphology has been observed at 823 K. While increasing the calcination temperature beyond 723 K, the precursor complexes may have adequate thermal energy to reorient themselves resulting lesser chance of agglomeration. In which the inorganic compounds decomposed completely and free from impurities in-turn a notable effect on the final morphology. Beyond 823 K, the morphology undergoes a transition from nanoclusters to macro grains. This may be ascribed to the subsequent growth of interconnected crystallites among the grain network, which favors the formation of larger micrometer-sized particles [23]. SEM studies are in good agreement with XRD results.

The crystallite size estimated from XRD studies is compared with the grain size obtained from SEM analysis and are listed in Table 1. The grain size obtained from the SEM images was found to be larger than the average crystallite size estimated from the XRD patterns because SEM visualizes the surface of NPs, which may contain more than one crystallite. Increase in the calcination temperature increased the crystallinity of the NPs, ultimately resulting in the increase in the grain size and the surface became smoother. Therefore the effect of calcination temperature and the specific route chosen for the synthesis have influenced the morphology. The 823 K sample was then chosen for TEM studies, because the grain growth was less enhanced than at 923 K. The TEM images disclosed that the formation of highly dispersed NPs (Fig. 5(a,b)) with arbitrary size and shape. Selective Area Electron Diffraction pattern (SAED) confirmed the polycrystalline nature of the system as shown in Fig. 5(c). To identify the elemental composition, EDS analyses was employed. Fig. 6(a) clearly showed that the sample was only composed of tungsten and oxygen and no other impurities were observed, which also supports the XRD results. The inset of Fig. 6(a) displays the atomic and weight percent of oxygen and tungsten.

FTIR spectra clearly identified the various mode of vibrations of the samples in the infrared regime (Fig. 6(b)). O-Lattice group was observed at 502 cm^{-1} . The typical band at 610 cm^{-1} was due to the γ (W–O–W) signal. The presence of stretching vibrations (W=O, W–O) of WO_3 NPs identified at 955 cm^{-1} . The vibration at 1401 cm^{-1} can be attributed to the presence of W–O functional group. The 1625 cm^{-1} band is assigned to the H–O–H bending vibration. Especially from the peak sited at 3449 cm^{-1} indicates the emergence of intercalated water molecules (W–OH $\cdot\cdot$ H_2O). These assignments found evidence for the formation of WO_3 NPs [24].

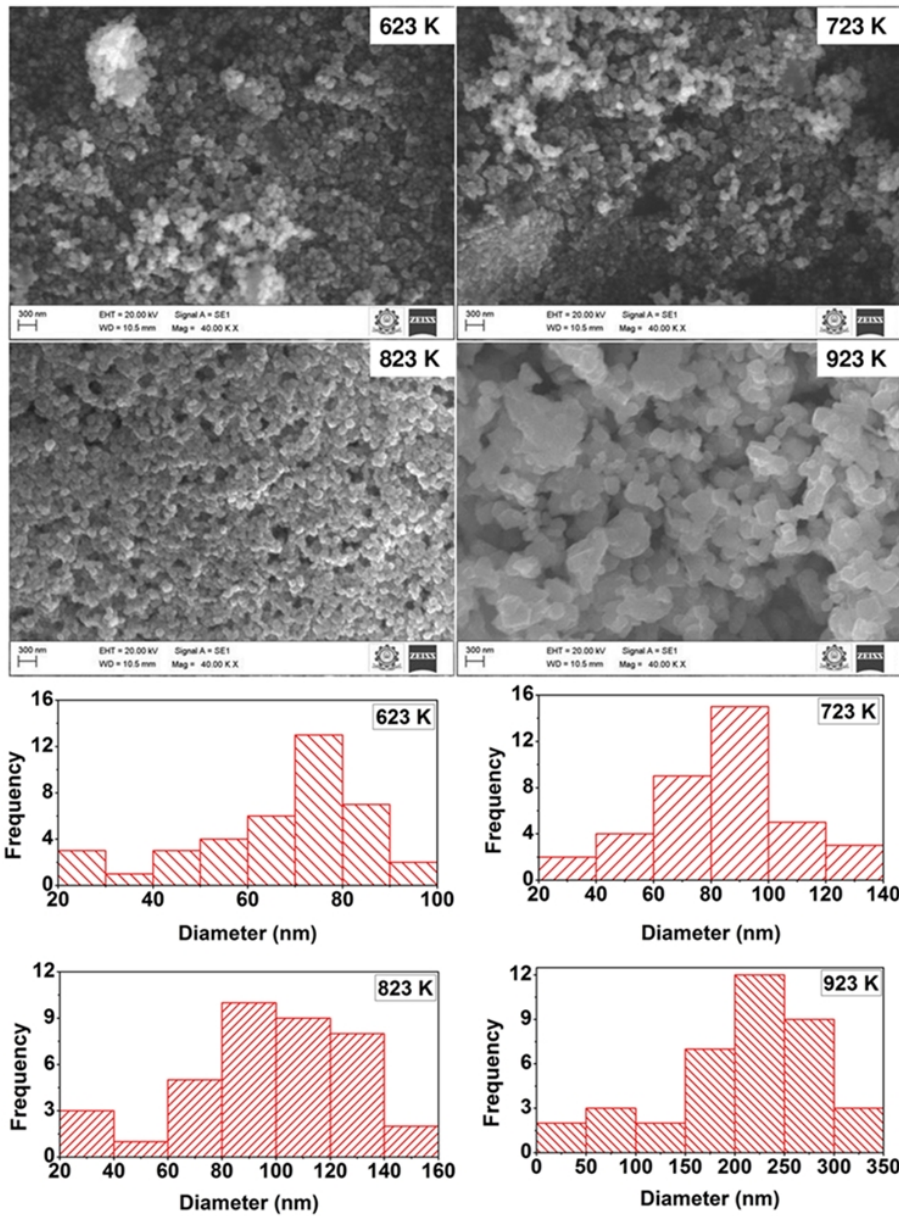


FIG. 4. SEM images and size distribution histograms of WO_3 NPs calcined at various temperatures

TABLE 1. Structural, morphological and optical parameters of the prepared WO_3 NPs

Samples	2θ (deg.)	FWHM (β) (deg.)	Crystallite size (D) (nm)	Grain size obtained from SEM (nm)	Optical band gap energy (eV)
623 K	–	–	–	75	2.76
723 K	23.6730	0.4783	17	86	2.65
823 K	23.7088	0.2292	35	104	2.55
923 K	23.5897	0.2080	39	233	2.48

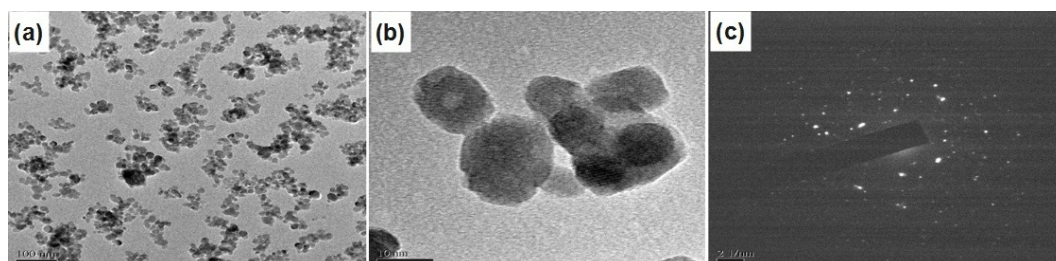
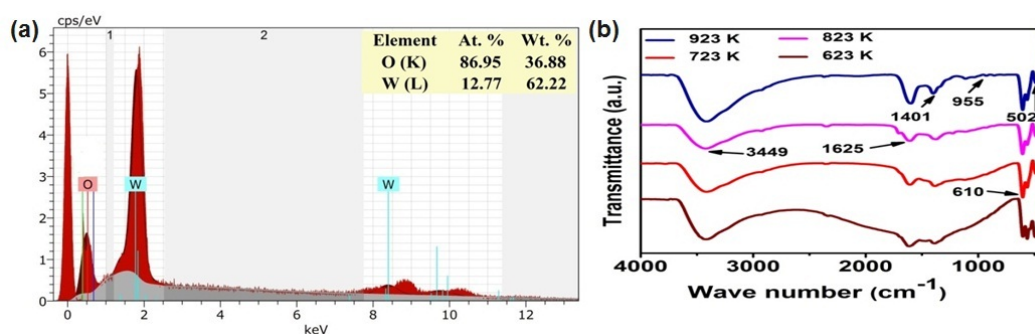


FIG. 5. (a,b) TEM images and (c) SAED pattern of the sample calcined at 823 K

FIG. 6. (a) EDS spectra of WO_3 NPs calcined at 823 K and (b) FTIR spectra of the prepared nanostructures

3.2. XPS analysis

Figure 7 shows the XPS spectra of pristine WO_3 samples calcined at various temperatures. The high resolution spectra of W4f- and O1s-levels have been acquired. The peak couples located at ~ 35.8 and 37.8 eV corresponding to $\text{W}4f_{7/2}$ and $\text{W}4f_{5/2}$ respectively, which are characteristic for W^{6+} oxidation state as shown in Fig. 7(a). It should be mentioned that these doublet peaks were typical for all specimens and that there were relative small changes in values.

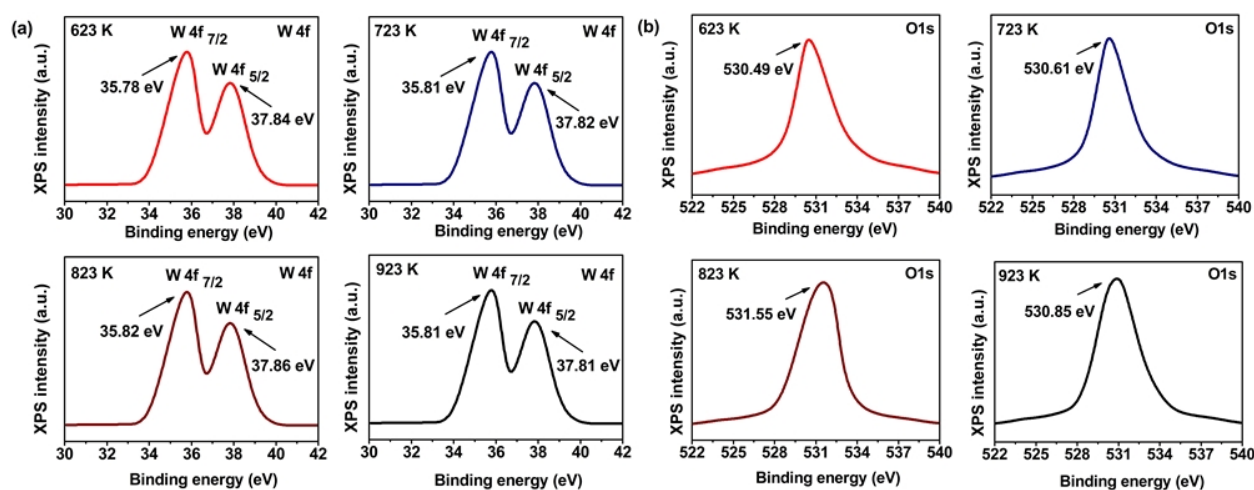


FIG. 7. (a) W4f and (b) O1s XPS spectra of the samples calcined at various temperatures (623–923 K)

The O1s peaks located at 530.49, 530.61 and 530.85 eV were attributed to lattice oxygen (O^{2-}) in WO_3 (Fig. 7(b)). While the peak at 531.55 eV (O1s of 823 K) is associated with O^{2-} of OH^- in the oxygen deficient regions within the matrix of WO_3 [25]. These oxygen vacancies are crucial for improving surface conductivity. In $m\text{-WO}_3$, the valence and conduction bands are comprised primarily of O 2p and W 5d states. The oxygen vacancies lead to outward motion of W atoms surrounding the vacancy i.e., relax away from the vacancy. On relaxation of internal coordinates,

the doubly occupied vacancy-induced states tend to move into the conduction band. As a result, two electrons then occupy the extended conduction-band states [26]. These investigations confirmed the successful formation of WO₃ NPs.

3.3. Optical studies

3.3.1. Evaluation of optical band gap. To explore the optical performance of the resulting NPs, UV-Vis spectroscopy was studied. As the calcination temperature increases, the absorption intensity in the visible region also increases as shown in Fig. 8(a). The sample calcined at 923 K showed absorption maximum at ~365 nm. Optical band gap of the prepared NPs was estimated from the Tauc's relation as shown in Eq. (7):

$$\alpha hv = k (hv - E_g)^{n/2}, \quad (7)$$

where α is the absorption coefficient, h is the Planck's constant, ν is the light frequency; k is a constant, E_g is the optical band gap, and $n = 1$ for direct transition and is 4 for allowed indirect transition. The band gap was calculated by extrapolating the linear portion of the plot of hv versus $(\alpha hv)^2$ curve to X-axis as shown in Fig. 8(a) (inset). A wide range of band gap from 2.48 to 2.76 eV has been observed, indicating that the samples were having tunable band gap (Table 1). Due to quantum confinement effect the band gap decreases with increasing particle size. The obtained band gap values were agreed well with WO₃ NPs reported in the literature [8].

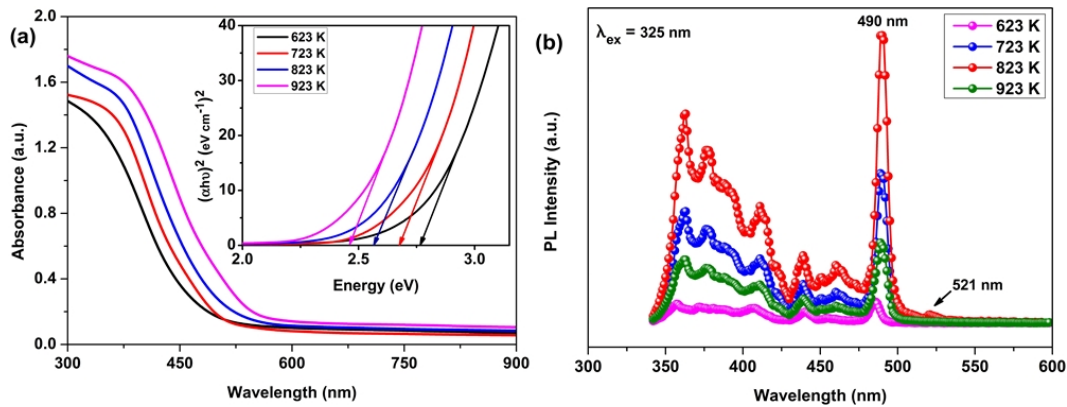


FIG. 8. (a) Absorbance spectra and Tauc's plot (inset) and (b) PL spectra of the prepared WO₃ samples

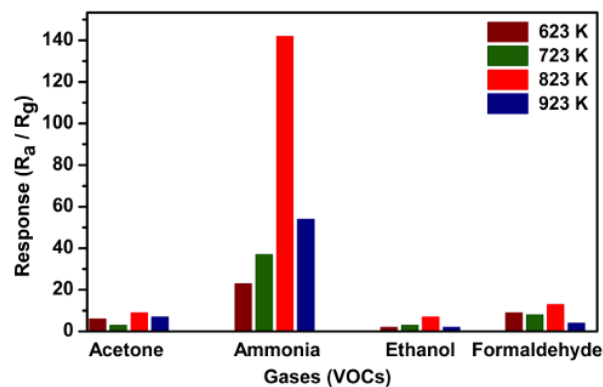


FIG. 9. Selectivity studies of the synthesised WO₃ samples (623 – 923 K)

3.3.2. Defect states. Figure 8(b) shows the PL signatures of the prepared samples at room temperature with the excitation wavelength of 325 nm. The peak found at 378 nm corresponds to NUV emission and is attributed to the recombination between the electron occupying the resonant defect state in conduction band and a hole in the valence band [27]. The emission at 412 nm may be allocated to the recombination of free excitons and is denoted as near band edge emission. The peak located at 459 nm suggesting that the electron hole pair separation rapidly, which may facilitate the electron transfer efficiency [28]. The blue emission at 490 nm can be assigned to oxygen vacancies

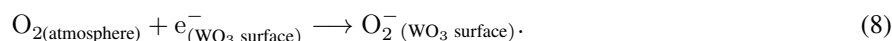
associated with defect level in the band gap for its electron transition [29]. As the calcination temperature of WO₃ NPs increases up to 823 K, the intensity of the oxygen vacancies related PL peak (490 nm) is found to increase and the further increase in calcination temperature is accompanied by a decrease in oxygen vacancies, while the relevant crystalline performance is improved by a decrease in bulk defects. Unambiguously, the WO₃ NPs calcined at 823 K has a significantly higher PL intensity compared to other samples, which suggests the higher recombination rate of photo-induced electron-hole pair. In addition, a green emission peak at 521 nm was observed in 823 K sample, which is related to doubly charged oxygen vacancy centers (v_0^{++}) located at the surface of the NPs. This emission may be associated with various luminescent centers, such as defect energy states due to oxygen vacancies as well as dangling bonds into NPs. On the other hand, no signal corresponds to green emission occur in the 623, 723 and 923 K samples. Furthermore, all other peaks are due to the defects from bulk WO₃ formation. The obtained PL results are in good agreement with XRD and XPS studies.

3.4. Gas sensing studies

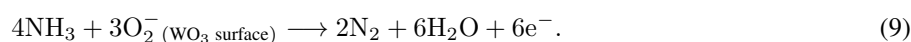
In order to find highly selective behavior, all the samples were tested as sensing materials in the presence of 200 ppm of various injected analytes like acetone, ammonia, ethanol and formaldehyde. All the samples show highly selective behavior to ammonia at room temperature while less sensitive to other gases, which purports pleasantly enough selective behavior of the prepared NPs as depicted in Fig. 9. Interestingly, the 823 K sample was highly selective ($S = 142$) towards 200 ppm ammonia. This behavior may be explained as follows. (i) Higher reducing capability of ammonia and lower kinetic diameter (0.326 nm) than that of other target gases promotes the diffusion process appreciably [30]. (ii) Lower ionization energy (10.18 eV), and also the dissociation of bond occurs at N–H with the significant dissociation energy of 314 kJ/mol [31], which are comparatively lower than other test gases in-turn the enhanced surface interactions [32]. (iii) Gas-solid interaction might be enhanced due to the lone pair of electrons in ammonia when the occurrence of H–N bond dissociation [5]. (iv) The diffusion of ammonia vapor within the Debye length has been excellently monitored by the cluster-like nanograin morphology of the NPs. (v) Good crystallinity associated with uniformly assembled surface morphology may acts as a percolation path for vapor diffusion. (vi) The presence of oxygen vacancies (as identified from the O1s spectra of 823 K) might have enhanced the reactive oxygen sites on the surface of WO₃ NPs and in turn improved gas–solid interaction. (vii) It is well known that oxygen vacancies had an obvious effect on improving the sensitivity. These vacancies act as electron donors, i.e., which introduce carriers in the conduction band of WO₃ thereby increasing the conductivity (as discussed in Section 3.2). (viii) The presence of green emission peak due to perturbed oxygen defect centers and larger surface defects (as observed through PL spectra of 823 K sample) might have improved the surface catalytic behavior and thereby resulting enhanced gas response. These intrinsic defects introduce more mid-gap states and largely enhance the transition probability of the valence electrons to its conduction band.

These notions supported explaining the significant ammonia response values reported in this literature, despite the large crystallite size resulting from the thermal treatment at 823 K.

When WO₃ is exposed to air ambience, the atmospheric oxygen species interact with the surface and chemisorbed as O₂[−] on the surface by capturing the electrons from the conduction band of WO₃ (Eq. (8)). It causes further increment in the surface resistance and this value could be fixed as the baseline resistance (R_a). This increased resistance would also develop a depletion region between the grain boundaries of the sample [33].



When the sensing material is exposed under the influence of reducing gas like ammonia, which interacts with adsorbed O₂[−] ions, this results in the liberation of electrons (Eq. (9)). Those released electrons have retained in the conduction band of the sensing material. As the width of the space charge region was decreased and leads to a decrease in surface resistance thereby attaining the steady state ammonia resistance (R_g). According to [34], the feasible interaction mechanism of WO₃ sensing surface towards atmospheric oxygen molecules and ammonia vapor at room temperature is as demonstrated in Eq. (9):



In case of recovery cycle, interacted ammonia gets desorbed and the sensor reached its baseline resistance. It accomplishes one proper cycle of response and recovery profile of the sensor.

The possible reasons for the low sensitive behavior of other samples (calcined at 623, 723 and 923 K) may be ascribed to various factors as follows: (i) the reduction in crystallinity would affect the gas diffusion and electron transport among the grain network, which would also have lowered the sensitivity of 623 and 723 K samples; (ii) beyond 823 K, the sensing response was found to be decrease, and it could be attributed to the agglomerated morphology of the NPs, however, higher calcination causes crystal grain growth in the sample, which would effectively modify

the microstructural properties of the NPs [35]. This might be affect the electron transfer during gas-solid interaction, resulting in a significant change (decrease) in the sensing response. (iii) Besides, the lack of oxygen vacancies (as observed from the O1s spectra of 623, 723 and 923 K) and poor oxygen defect centers (as identified from PL spectra) reduce the reactive oxygen adsorption sites on the sensing surface thereby lowering the sensor kinetics. The transient resistance response characteristics of the 823 K NPs were investigated towards ammonia in the range of 5 – 200 ppm as shown in Fig. 10. Inventingly, the sensing response was found to be 7 for 10 ppm of ammonia. Thus, it could be possible to detect ammonia even at low concentration levels under room temperature ambience and thus chiefly desired. The 823 K NPs also showed a high response of 18 towards 25 ppm ammonia while it increased to 142 in the presence of 200 ppm ammonia. When the concentration of ammonia vapor was increased from 5 to 1000 ppm, a very steep increase was observed in sensing response as depicted in Fig. 11(a). This trend is paramount factor for designing readout signal circuits and also applied in the construction of low-power gas sensing devices. Beyond 1000 ppm, the sensing response was found to be saturated, which may be due to the formation of multilayers of ammonia. These layers might affect the further gas – solid interaction by decreasing the active sites present in the sensor surface [36]. The lowest detection limit of the sensor towards ammonia gas was experimentally found to be 5 ppm. The saturation in sensor resistance is illustrated using a step change plot as shown in Fig. 11(b).

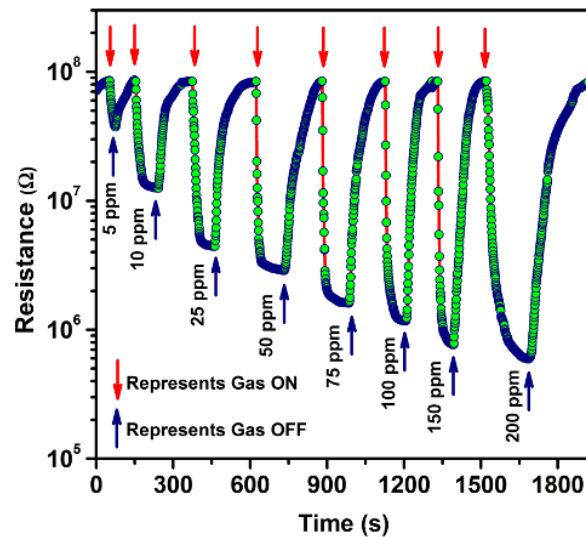


FIG. 10. Transient resistance response of 823 K sample towards different ammonia concentrations (5 – 200 ppm)

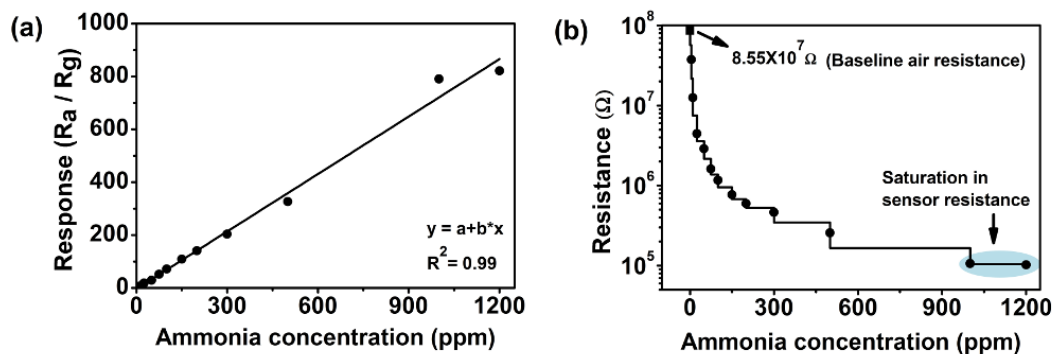


FIG. 11. (a) Response trend of 823 K sample towards various concentrations (5 – 1200 ppm) of ammonia at room temperature and (b) Change in electrical resistance as a function of ammonia concentration from its initial baseline resistance

The 823 K NPs exhibited quick response and recovery profile towards 200 ppm of ammonia as shown in Fig. 12. The response and recovery times were found to be 26 and 79 s respectively. Repeatable behavior of the 823 K sample

was investigated towards 200 ppm ammonia for three cycles. The repeatability was found to be excellent over the three evaluation cycles and displayed in Fig. 13(a). The sample also exhibited better stability towards 200 ppm of ammonia for a period of 50 days in the interval of 10 days as illustrated in Fig. 13(b) and showed only 4.22 % change (decrease) in sensitivity over 50 days.

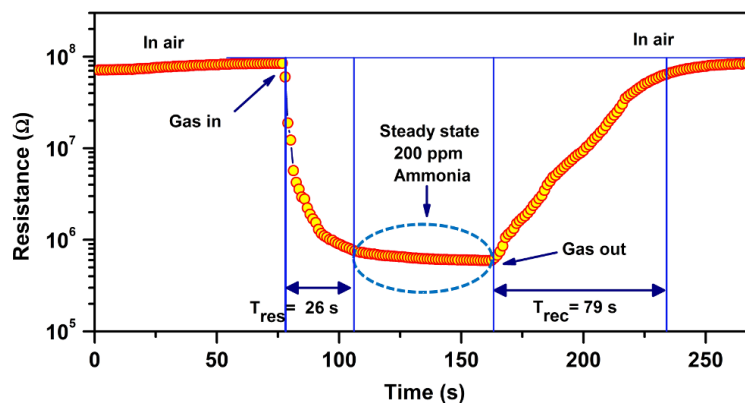


FIG. 12. Response-recovery profile of 823 K sample towards 200 ppm of ammonia

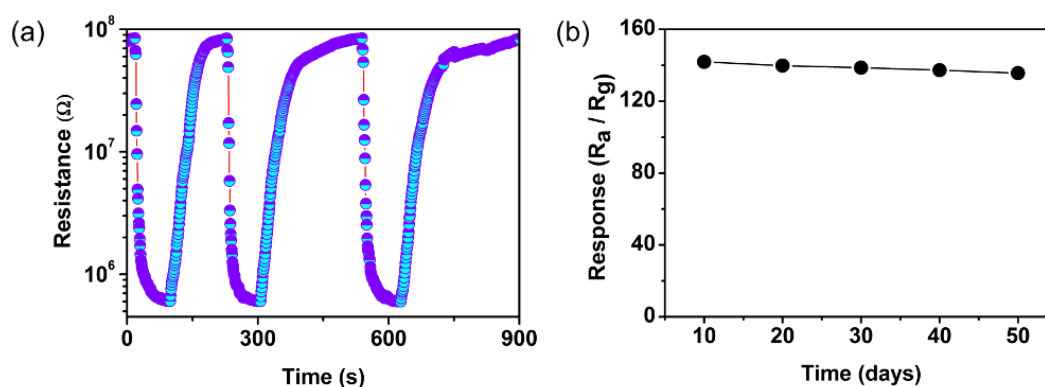


FIG. 13. (a) Repeatability and (b) Stability of 823 K sample towards 200 ppm of ammonia

To highlight the feature of the present study, the ammonia sensing performance of the NPs reported in this literature is compared with the available reports in Table 2.

4. Conclusion

The following conclusions can be drawn from the study results.

(1) Polycrystalline m-WO₃ NPs were synthesized by precipitation method and are employed as an effective sensing material in the fabrication of gas sensor towards different analytes, particularly ammonia. (2) Targeting ammonia vapor and operation at room temperature, the optimum calcination temperature was determined to be 823 K and the sensor based on 823 K sample showed a high response of 7 towards 10 ppm of ammonia, while it increased to 142 towards 200 ppm of ammonia with rapid response and recovery times of 26 and 79 s respectively. (3) Satisfying active detection range (5 – 1200 ppm), repeatability and long-term stability were ensured. (4) Improved crystallinity, well-ordered nanocluster like morphology, enhanced electron transfer efficiency due to intrinsic defects, presence of oxygen vacancies and the perturbed oxygen defect centers would effectively support the enhanced sensing behavior of the 823 K sample. (5) This study disclosed that the thermal treatment has to be altered to change the crystallinity and morphology of the pristine WO₃ NPs resulting in improved sensitivity.

The most noteworthy aspect is that all the excellent gas sensing performance of the WO₃ gas sensor was achieved at room temperature. This innovation disclosed the following significant possibilities: (i) the reported sensor can be used as an eminent gas sensing tool to contribute in many real-time applications such as diagnosis breath analysis systems, food and beverage sectors owing to its excellent figure of merits; (ii) the present work is completely free from the requirements of stabilizing agents and inbuilt micro heaters.

TABLE 2. Comparison of ammonia sensing performances of the present work with other reports

Material	Response	Concentration (ppm)	Response time (s)	Recovery time (s)	Temperature (K)	Ref.
WO ₃	5.5 ^a	100	18.3	91.2	648	[37]
WO ₃	9.7 ^a	1500	7	8	523	[38]
WO ₃	5.5 ^d	100	1	5	473	[39]
PANI	2.3 ^d	100	120	300	298	[40]
ZnO/ native-graphite	12 ^c	40–45	510	420	303	[41]
ZnO	1.43 ^a	5	30	450	503	[42]
ZnO	17 % ^b	100	51	160	303	[43]
ZnO	10 % ^b	25	49	19	303	[44]
WO ₃	142 ^a	200	27	77	303	This work

$${}^a S = \frac{R_a}{R_g}, \quad {}^b S = \frac{(R_0 - R_g)}{R_0} \times 100 \%, \quad {}^c S = \frac{R_a - R_g}{R_a}, \quad {}^d S = \frac{R_g}{R_a}.$$

References

- [1] Agency for toxic substances and disease (ASTDR) Registry, Public Heal. Statement Ammon. 2004, CAS# 7664–41–7, **1** (n.d.).
- [2] Erisman J.W., Sutton M.A., et al. How a century of ammonia synthesis changed the world. *Nat. Geosci.*, 2008, **1**, P. 636–639.
- [3] Malins C., Doyle A., et al. Personal ammonia sensor for industrial environments. *J. Environ. Monit.*, 1999, **1**, P. 417–422.
- [4] Alarie Y. Dose–response analysis in animal studies: prediction of human responses. *Environ. Health Perspect.*, 1981, **42**, P. 9–13.
- [5] Mani G.K., Rayappan J.B.B. A highly selective room temperature ammonia sensor using spray deposited zinc oxide thin film. *Sens. Actuators B Chem.*, 2013, **183**, P. 459–466.
- [6] Timmer B., Olthuis W., Berg A.V.D. Ammonia sensors and their applications – A review. *Sens. Actuators B. Chem.*, 2005, **107** (2), P. 666–677.
- [7] Parthasarathy Srinivasan, Madeshwari Ezhilan, et al. Room temperature chemiresistive gas sensors: challenges and strategies – a mini review. *Journal of Materials Science: Materials in Electronics*, 2019, **30**, P. 15825–15847.
- [8] Reza Abazari, Ali Reza Mahjoub, et al. Characterization and optical properties of spherical WO₃ nanoparticles synthesized via the reverse microemulsion process and their photocatalytic behavior. *Materials letters*, 2014, **133**, P. 208–211.
- [9] Llobet E., Molas G., et al. Fabrication of Highly Selective Tungsten Oxide Ammonia Sensors. *Journal of The Electrochemical Society*, 2000, **147** (2), P. 776–779.
- [10] Wood V., Panzer M.J., et al. Selection of Metal Oxide Charge Transport Layers for Colloidal Quantum Dot LEDs. *ACS Nano*, 2009, **3** (11), P. 3581–3586.
- [11] Lidia Santos, Celia Silveira, et al. Synthesis of WO₃ Nanoparticles for Biosensing Applications. *Sensors and Actuators B Chemical*, 2015, **223**, P. 186–194.
- [12] Jinhui Wang, Liu G., Youwei Du. Mechanochemical synthesis of sodium tungsten bronze nanocrystalline powders. *Materials Letters*, 2003, **57** (22–23), P. 3648–3652.
- [13] Haidong Zheng, Jian Zhen Ou, et al. Nanostructured Tungsten Oxide-Properties, Synthesis, and Applications. *Adv. Funct. Mater.*, 2011, **21**, P. 2175–2196.
- [14] Guan Wang, Yuan Ji, et al. Fabrication and Characterization of Polycrystalline WO₃ Nanofibers and Their Application for Ammonia Sensing. *J. Phys. Chem. B*, 2006, **110**, P. 23777–23782.
- [15] Zuquan Wu, Xiangdong Chen, et al. Enhanced sensitivity of ammonia sensor using graphene/polyaniline nanocomposite. *Sensors and Actuators B*, 2013, **178**, P. 485–493.
- [16] Liu H., Shen W., Chen X. A room temperature operated ammonia gas sensor based on Ag-decorated TiO₂ quantum dot clusters. *RSC Adv.*, 2019, **9**, P. 24519–24526.
- [17] Wang C.-Y., Zhang X., et al. Ammonia sensing by closely packed WO₃ microspheres with oxygen vacancies. *Chemosphere*, 2018, **204**, P. 202–209.
- [18] Tai H., Jiang Y., et al. Fabrication and gas sensitivity of polyaniline–titanium dioxide nanocomposite thin film. *Sensors and Actuators B: Chemical*, 2007, **125**, P. 644–923.
- [19] Li C.F., Hsu C.Y., Li Y.Y. NH₃ sensing properties of ZnO thin films prepared via sol–gel method. *J. Alloys Compd.*, 2014, **606**, P. 27–31.
- [20] Martinez-de la Cruz A., Sanchez Martinez D., Lopez Cuellar E. Synthesis and characterization of WO₃ nanoparticles prepared by the precipitation method: Evaluation of photocatalytic activity under vis–irradiation. *Solid State Sciences*, 2010, **12**, P. 88–94.
- [21] Ahmadi M., Sahoo S., et al. WO₃ nano-ribbons: Their phase transformation from tungstite (WO₃·H₂O) to tungsten oxide (WO₃). *J. Mater. Sci.*, 2014, **49** (17), P. 5899–5909.
- [22] Parthasarathy Srinivasan, John Bosco Balaguru Rayappan. Growth of Eshelby twisted ZnO nanowires through nanoflakes & nanoflowers: A room temperature ammonia sensor. *Sensors & Actuators: B. Chemical*, 2018, **277**, P. 129–143.

- [23] Chen D., Sugahara Y. Tungstate-Based Inorganic-Organic Hybrid Nanobelts/Nanotubes with Lamellar Mesostructures: Synthesis, Characterization, and Formation Mechanism, *Chem. Mater.*, 2007, **19**, P. 1808–1815.
- [24] Diaz-Reyes J., Dorantes-García V., Perez-Benítez A., Balderas-Lopez J.A. Obtaining of films of tungsten trioxide (WO₃) by resistive heating of a tungsten filament. *Superficies y Vacío.*, 2008, **21** (2), P. 12–17.
- [25] Jie Li, Yuan Liu, et al. A full-sunlight-driven photocatalyst with super long-persistent energy storage ability. *Sci. Rep.*, 2013, **3** (2409), P. 1–6.
- [26] Wang W., Janotti A., Van de Walle C.G. Role of oxygen vacancies in crystalline WO₃. *J. Mater. Chem. C*, 2016, **4**, P. 6641–6648.
- [27] Kriti, Puneet Kaur, et al. Influence of defect structure on colour tenability and magneto optical behaviour of WO₃ nanoforms. *RSC Adv.*, 2019, **9**, P. 20536–20548.
- [28] Jeyapaul T., Prakash K., et al. Synthesis of WO₃ nanorods and their photocatalytic degradation of organic contaminants. *Rasayan J. Chem.*, 2018, **11** (4), P. 1405–1414.
- [29] Mohammed Harshulkhan S., Janaki K., et al. Structural and optical properties of Ag doped tungsten oxide (WO₃) by microwave-assisted chemical route. *J. Mater Sci: Mater. Electron.*, 2016, **27**, P. 3158–3163.
- [30] Arockia Jayalatha Kulandaisamy, Jonnala Rakesh Reddy, et al. Room temperature ammonia sensing properties of ZnO thin films grown by spray pyrolysis: Effect of Mg doping. *Journal of Alloys and Compounds*, 2016, **688**, P. 422–429.
- [31] Dill J.D., Allen L.C., Topp W.C., Pople J.A. Systematic study of the nine hydrogen-bonded dimers involving ammonia, water, and hydrofluoric acid. *J. Am. Chem. Soc.*, 1975, **97**, P. 7220–7226.
- [32] Nayak A.K., Ghosh R., et al. Hierarchical nanostructured WO₃-SnO₂ for selective sensing of volatile organic compounds. *Nanoscale*, 2015, **7**, P. 12460–12473.
- [33] Barsan N., Weimar U. Conduction Model of Metal Oxide Gas Sensors. *J. Electroceramics*, 2001, **7**, P. 143–167.
- [34] Jeevitha G., Abhinaya R., et al. Porous reduced graphene oxide rGO/WO₃ nanocomposites for the enhanced detection of NH₃ at room temperature. *Nanoscale Adv.*, 2019, **1**, P. 1799–1811.
- [35] Wang H., Quan X., Zhang Y., Chen S. Direct growth and photoelectrochemical properties of tungsten oxide nanobelt arrays, *Nanotechnology*, 2008, **19** (065704), P. 1–6.
- [36] Patil D.R., Patil L.A., Amalnerkar D.P. Ethanol gas sensing properties of Al₂O₃-doped ZnO thick film resistors. *Bulletin of Materials Science*, 2007, **30**, P. 553–559.
- [37] Yan A., Xie C., et al. Synthesis, formation mechanism and sensing properties of WO₃ hydrate nanowire netted-spheres. *Materials Research Bulletin*, 2010, **45** (10), P. 1541–1547.
- [38] Nguyen Van Hieu, Vu Van Quang, Nguyen Duc Hoa, Dojin Kim. Preparing large-scale WO₃ nanowire-like structure for high sensitivity NH₃ gas sensor through a simple route. *Curr. Appl. Phys.*, 2011, **11**, P. 657–661.
- [39] Ji-yan Leng, Xiu-juan Xu, et al. Synthesis and gas-sensing characteristics of WO₃ nanofibers via electrospinning. *Journal of Colloid and Interface Science*, 2011, **356**, P. 54–57.
- [40] Sengupta P.P., Kar P., Adhikari B. Influence of dopant in the synthesis, characteristics and ammonia sensing behavior of processable polyaniline. *Thin Solid Films*, 2009, **517**, P. 3770–3775.
- [41] Tulliani J.M., Cavalieri A., et al. Room temperature ammonia sensors based on zinc oxide and functionalized graphite and multi-walled carbon nanotubes. *Sensors and Actuators B*, 2011, **152**, P. 144–154.
- [42] Siril V.S., Madhusoodanan K.N., Rajan S.K., Louis G. Study on ammonia gas sensing property of hydrothermally synthesized pure ZnO nanorods. *AIP Conf. Proc.*, 2017, **1849**, 020033.
- [43] Andre R., Kwak D., et al. Sensitive and Selective NH₃ Monitoring at Room Temperature Using ZnO Ceramic Nanofibers Decorated with Poly(styrene sulfonate). *Sensors*, 2018, **18** (1058), P. 1–13.
- [44] Venkatesh P.S., Dharmaraj P., et al. Point defects assisted NH₃ gas sensing properties in ZnO nanostructures. *Sens. Actuators B Chem.*, 2015, **212**, P. 10–17.